A New InSAR Persistent Scatterer Selection Technique Using Top Eigenvalue of Coherence Matrix

Sankarambadi Navneet, Jin-Woo Kim, and Zhong Lu, *Senior Member, IEEE*

***Abstract*— Differential interferometric synthetic aperture radar (InSAR) time-series processing relies on identifying coherent pixels in SAR image stacks that show the persistent scatterer (PS) or distributed scatterer (DS) behavior. Accuracy of InSAR time-series estimates is dependent on the quality of selected PS/DS pixels. Current pixel selection techniques perform well when identifying highly coherent pixels but produce many false alarms in low coherence regions due to the inherent bias in residual phase estimation. Therefore, pixels with low coherence may have the appearance of noise and be rejected if the coherence threshold is too high. In contrast, lowering the threshold increases the number of false alarms introduced in processing giving noisier time-series as a result of incorrect phase unwrapping. The multidimensional SAR data acquisition can be described as a zero mean Gaussian process fully described by the covariance matrix. In this paper, we investigate the covariance matrix using a random matrix theory approach to find the statistical properties of the eigenvalues for simulated and real SAR data. The probability distribution of all the eigenvalues in this case is limited by the Marcenko–Pastur distribution. The histogram of the highest eigenvalue follows a Tracy–Widom distribution. Thus, by adopting a pixel selection strategy based on a threshold on the highest eigenvalue of the coherence matrix, we can differentiate between low coherence and noise pixels. In addition, our technique provides a methodology to detect the number of targets present in multiscatterer layover pixels and extract time-series information from double bounce response of bridges. Applying the technique for TerraSAR-X data over Berlin shows the effectiveness of the algorithm.**

***Index Terms*— Differential interferometric synthetic aperture radar (DInSAR), eigenvalue decomposition (EVD), persistent scatterer (PS) technique, random matrix theory, time-series processing.**

I. Introduction

SATELLITE interferometric synthetic aperture radar (InSAR) provides the perfect tool for measuring millimeter-level ground displacement over wide swaths of land on the Earth's surface with low-latency revisit periods in all-weather conditions [1], [2]. The magnitude of cross correlation between two coregistered SAR image acquisitions is known as the coherence of the differential InSAR (DInSAR) pixel and its phase is the interferometric quantity, which gives the deformation within that period [3]. Assuming the stationarity and ergodicity of SAR image pixel acquisitions, the empirical coherence is calculated by averaging within a window of neighboring pixels. This empirical coherence is a measure of the extent of decorrelation for a pixel primarily due to temporal and geometric (baseline) degradation/decorrelation [4]. The magnitude of phase noise for an interferometric pixel is proportional to the decrease in coherence [5]. While the DInSAR has proven very effective in measuring numerous deformation phenomena [6]–[9], temporal decorrelation due to an incoherent movement of individual scattering elements limits its applicability to observe long-term trends. The persistent scatterer InSAR (PSI) technique [10]–[13] is based on identifying a coherent radar signal (PS) in a stack of topography-compensated interferograms and discriminating them from incoherent contributions, to measure the temporal evolution of interferometric phase of targets with physical manifestation. Reference [9] shows a statistical relationship between the amplitude dispersion index ($D_A = \sigma_A/\mu_A$, where μ_A is the mean and σ_A is the standard deviation of the amplitude of a pixel in the SAR image stack) and the interferometric phase standard deviation (σ_ϕ), which suggests that for pixels having high signal-to-noise ratio (SNR) and exhibiting a stable phase, $D_A \approx \sigma_\phi$. After the initial selection based on ($D_A < 0.3$), an *a priori* deformation model is applied to further weed out pixel candidates whose phase in time shows large deviations from expected behavior. However, in many cases [14], the deformation of scatterers is unknown *a priori*. In Stanford method for persistent scatterers (StaMPS), phase values for individual candidates are filtered assuming that deformation is spatially correlated with neighboring candidates. The residual phase values over multiple interferograms are used to derive a measure called temporal coherence, γ_x. Candidate pixels are qualified as a PS based on a threshold of the temporal coherence ($\gamma_x > 0.3$). The StaMPS method uses a relaxed ($D_A < 0.6$) limit for initial candidate selection, to allow for detecting a PS having high dispersion index but low phase variance. To mitigate the long-term decorrelation effects, which result in a poor estimate of the deformation time-series of the PS, the small baselines subset (SBAS) approach [15] uses only short (temporal and spatial) baseline pairs of SAR images for the time-series analysis. Although more number of PS are detected

Manuscript received July 3, 2017; revised October 22, 2017; accepted November 2, 2017. Date of publication December 4, 2017; date of current version March 23, 2018. This work was supported in part by the National Aeronautics and Space Administration (NASA) Earth and Surface Interior Program under Grant NNX16AL10G, in part by the NASA Interdisciplinary Research in Earth Science (IDS) Program under Grant 80NSSC17K0022, and in part by the Shuler-Foscue Endowment at Southern Methodist University. *(Corresponding author: Zhong Lu.)*

S. Navneet was with the Roy M. Huffington Department of Earth Sciences, Southern Methodist University, Dallas, TX 75275 USA. He is now with Capella Space Corporation, Palo Alto, CA 94303 USA.

J.-W. Kim and Z. Lu are with the Roy M. Huffington Department of Earth Sciences, Southern Methodist University, Dallas, TX 75275 USA (e-mail: zhonglu@smu.edu).

Color versions of one or more of the figures in this paper are available online at http://ieeexplore.ieee.org.

Digital Object Identifier 10.1109/TGRS.2017.2771386

by this technique without the need for an *a priori* deformation model, StaMPS is more suited for processing InSAR data, assuming pointlike scatterers over urban areas which are dominated by a large presence of stable man-made targets. Pixels corresponding to natural targets having low temporal coherence and pixels containing multiple targets are missed.

A group of pixels corresponding to a large geophysical target, such as outcrops or natural terrain, covered by sparse vegetation may have low temporal coherence but share similar backscattering statistics [statistically homogeneous pixels (SHPs)]. In the SqueeSAR [16], a nonparametric test [two-sample Kolmogorov–Smirnov test (KS test)] is employed to identify SHPs (pixels having similar amplitude distribution over the stack of SAR images). The coherence matrix for these SHPs is calculated from the SAR data stack and used for filtering the interferograms prior to phase unwrapping. If individual SHP phase measurements are noisy but the spatially adaptive filtering estimate is stable as indicated by a goodness-of-fit measure (γ_{PTA}), then these pixels together are known as distributed scatterers (DSs). Unlike the SBAS in which only short baseline pairs of interferograms are permitted, the SqueeSAR uses all available interferogram combinations with appropriate weighting. Essentially, the DS is a group of pixels together showing a single scattering behavior. In this way, in addition to those pixels identified as a PS, an increase in the number of measurement points due to the DS is obtained especially for nonurban areas.

In urban areas, unlike the DS, we encounter many pixels affected by layover of multiple scatterers at different elevations but registered at the same cross range [17]–[20]. Due to the multibaseline nature of SAR acquisitions, a target scatterer occupying a range–azimuth resolution pixel is observed from slightly different viewing angles every acquisition. SAR tomography [21]–[23] entails reconstructing the reflectivity profile for this target scatterer in the elevation direction by synthesizing an aperture from nonuniformly spaced samples of the observed complex backscattering distribution by assuming a certain structure of the elevation response [24], [25]. Numerous techniques for the elevation aperture synthesis include classical beamforming, performing the Fourier transform on the interpolated data, and spectral estimation techniques, such as singular value decomposition inversion among others. SAR tomography has proved successful in performing 3-D (range–azimuth height)/4-D (range–azimuth-height-deformation rate) SAR imaging [26] and in distinguishing multiple scatterers present in pixels affected by layover phenomena. However, due to the specific structure assumed for a targets response, precise phase calibration with respect to atmospheric artifacts and nonlinear errors is needed prior to performing tomographic inversion.

Unlike the SAR tomographic inversion techniques mentioned previously, Component extrAction and sElection SAR (CAESAR) [27] does not impose a specific structure on the elevation response of a scatterer. Instead, it exploits the principal component analysis (PCA) technique to find the eigenvector direction in the coherence matrix with the most average power and hence can be implemented directly at the interferogram generation stage. Eigenvalue decomposition (EVD) is performed to calculate the eigenvalue spectrum of the coherence matrix. Similar to the SqueeSAR, spatially adaptive multilooking is employed to estimate the coherence matrix. The eigenvector corresponding to the top eigenvalue is the direction in the data giving information about the presence of a primary scattering mechanism. In the case of layover, a secondary scattering mechanism is represented by next highest eigenvalue–eigenvector pair. The original interferometric phase is replaced by the phase of an eigenvector corresponding to the highest eigenvalue effectively reducing phase noise due to interference from eigenvalues representing decorrelation.

Even though this technique is effective in separating multiple scatterers within a pixel, we are still presented with the challenge of identifying the number of scatterer targets present in a given pixel (zero in noise pixels, one in the PS and the DS, two or more in multiscatterer pixels) based on the eigenvalue spectrum of the empirical coherence matrix. One method is to perform CAESAR processing on pixel candidates with low phase variance ($\gamma_x > 0.3$) to avoid selecting noisy pixels. The eigenvalue spectrum should be composed of few large eigenvalues (corresponding to the number of scatterer targets) and rest of eigenvalues (corresponding to decorrelation) equal to the noise variance (σ^2). Many techniques exist such as the Kaiser–Guttman greater-than-one rule [29] in which the eigenvalues above a certain threshold (the average variance of empirical data) corresponds to the number of targets. The methodology works for high coherence pixels (having a dominant eigenvalue) but overestimates the number of target scatterers in low coherence regions. This is because the empirical coherence matrix is a biased overestimate of the true coherence affected by the finite estimation window size. Therefore, even when the coherence matrix represents noise pixels, their eigenvalues may exceed the threshold merely by statistical fluctuations. Incorrect pixel selection procedure consequently impacts phase estimation resulting in poor phase unwrapping and noisy time-series estimates.

In this paper, we formulate a pixel selection strategy for time-series InSAR processing using recent advances in the random matrix theory [28], [29]. The literature on this subject has dealt extensively with obtaining analytical solutions for the asymptotic behavior of the joint probability distribution (jpdf) of eigenvalues for covariance matrices of randomly generated data [30]. Particularly, we are interested in knowing how the eigenvalue spectrum of the coherence matrix for pixels corresponding to noise contrasts with pixels having one or more stable targets. This allows us to distinguish low coherence pixels from noise pixels and correctly determine the number of targets present in layover affected pixels at the interferogram generation stage itself.

This paper is organized as follows. In Section II, we develop a statistical description of multibaseline, multitemporal SAR data. In Section III, we investigate the coherence matrix using the random matrix theory to find the statistical response of the eigenvalues for simulated and real SAR data. A pixel selection technique based on the statistics of the top eigenvalue is adopted. We show that our technique achieves better candidate selection compared with the amplitude dispersion index and StaMPS. In Section IV, the time-series analysis of

SAR data over Berlin demonstrates the significant increase in measurement points our candidate selection technique achieves in low coherence regions. The observed time-series deformation is briefly discussed. Section V draws the conclusions of this paper.

II. Multidimensional SAR Signal Model

We begin our analysis with the signal characterization for 4D-SAR imaging as assumed in CAESAR [27]. Consider a stack of N coregistered SAR images each obtained at time intervals t_i with a spatial baseline of b_i relative to single master acquisition, $i = 0, 1, 2, \ldots, N-1$. The received signal x for transmitted wavelength λ in each range–azimuth-focused pixel is the combined scattering response of targets present at different elevations h_i but equivalent cross-range R to the sensor, undergoing deformation in the line-of-sight (LoS) direction with a velocity v_j, in the matrix form is given as

$$x = A\Upsilon \tag{1}$$

where $\Upsilon = [\Upsilon_0, \Upsilon_1, \Upsilon_2, \ldots, \Upsilon_{M-1}]^{\text{tr}}$ is the collection of backscattering distribution at M discrete bins associated with discrete samples (h_i, v_j), distributed over the elevation/velocity range of interest. "tr" is the transpose operator. $A = \sqrt{N}[a_0, a_1, a_2, \ldots, a_{M-1}]$ is the $N \times M$ matrix collecting the steering vectors a_m

$$a_m = \frac{e^{[-j2\pi(\psi h_i + \eta v_j)]}}{\sqrt{N}}.$$

For which, $\psi = [\psi_0, \psi_1, \psi_2, \ldots, \psi_{N-1}]^{\text{tr}}$, $\psi_i = ((2b_i)/(\lambda R \sin(\theta)))$ (sampling frequency in the elevation direction), where b_i is the perpendicular baseline and θ is the incidence angle. $\eta = [\eta_0, \eta_1, \eta_2, \ldots, \eta_{N-1}]^{\text{tr}}$, $\eta_i = \frac{2t_i}{\lambda}$ (temporal frequency), where t_i is the temporal baseline.

Assuming the presence of a scatterer at $(\hat{h}, \hat{v})$ for a pixel in the multibaseline data, the inversion of the scattering matrix involves the calculation of the covariance matrix

$$\begin{aligned}(\hat{h}, \hat{v}) &= \text{argmax } E\{(a^H x)(a^H x)^H\} \\ &= \text{argmax } a^H E\{xx^H\}a \\ &= \text{argmax } a^H C a\end{aligned}$$

where H stands for a Hermitian operator, and $C = E\{xx^H\}$ is the covariance matrix estimated from the original complex data x, and E is the expectation operator.

In the subsequent analysis, we consider the coherence matrix T obtained by normalizing the complex SAR observations to avoid any estimation errors due to amplitude disturbances in the data $y_i = (x_i/(E[|x_i|^2])^{1/2})$.

In the urban scenario, the backscattering statistics of pixels are closely related to the geometry of urban structures they represent. For this reason, using a rectangular window for spatial correlation will degrade the measured coherence by introducing nonhomogenous and neighboring noise pixels in the estimation. Several studies in SAR polarimetry exploit the amplitude statistics for a pixel in a stack of SAR images over the period of acquisition to find similar neighboring pixels, SHPs. This technique of spatial adaptive filtering allows preserving the image details. In this paper, we use the two-sample Anderson–Darling (AD) test. The AD test is suited to long-tailed scattering distributions, which are more representative of SAR pixel temporal amplitude fluctuations in comparison with the more widely used KS test, which places more emphasis on the bulk of the distribution. It generally outperforms the KS test and other similar tests when applied to high-resolution SAR images with different types of scatterers. For an exhaustive discussion on the different techniques, please refer to [31].

The empirical coherence matrix for a pixel is given as

$$T = E[yy^H] = \frac{\sum_{y \in \text{SHP}} yy^H}{L} \tag{2}$$

where L is the total number of neighboring pixels found similar to the pixel under consideration using the AD test.

The magnitude of empirical coherence $(\tilde{\gamma}_{(i,j)})$ is the measure of correlation between acquisitions $(i, j = 1, 2, \ldots, N)$, wheares the angle component $(\phi_{(i,j)})$ gives the differential interferometric phase

$$T = \begin{bmatrix} 1 & \tilde{\gamma}_{1,N} e^{j\tilde{\phi}_{1,2}} & \cdots & \tilde{\gamma}_{1,N} e^{j\tilde{\phi}_{1,N}} \\ \tilde{\gamma}_{2,1} e^{j\tilde{\phi}_{2,1}} & 1 & \cdots & \tilde{\gamma}_{2,N} e^{j\tilde{\phi}_{2,N}} \\ \vdots & \vdots & \ddots & \vdots \\ \tilde{\gamma}_{N,1} e^{j\tilde{\phi}_{N,1}} & \tilde{\gamma}_{N,2} e^{j\tilde{\phi}_{N,2}} & \cdots & 1 \end{bmatrix}. \tag{3}$$

For a series of acquisitions, SAR image pixels generally show multivariate Gaussian characteristics [32]. In this case, the coherence matrix (T) fully describes the data and follows a Wishart distribution. It is a Hermitian positive semidefinite matrix having real eigenvalues.

The EVD allows for the decomposition of the full rank N-dimensional coherence matrix such that

$$T = \sum_{i=1}^{N} \Lambda_i u_i u_i^H \tag{4}$$

where $\Lambda_i = 1, 2, \ldots, N$ are the eigenvalues of the coherence matrix arranged in the descending order and $u_i = 1, 2, \ldots, N$ are the corresponding eigenvectors.

In this paper, we consider 27 high-resolution spotlight SAR images (0.6-m range resolution and 1.1-m azimuth resolution) acquired by a TerraSAR-X (X-band, $\lambda = 31$ mm) satellite sensor over the Eisenbahn bridge, Berlin in orbit 55, beam 57 (ascending track), from February 2008 to December 2009. Fig. 1 shows the SAR amplitude image of the study area in Berlin.

III. Pixel Selection Strategy

A. Coherence Matrix Analysis

Our null model consists of simulating the coherence matrix for data containing small random entries corresponding to pure noise. This was simulated through a Monte Carlo process by calculating random values belonging to a zero mean circular complex Gaussian distribution. The coherence matrix in this case is given by a Wishart matrix. From real data, we choose pixels (Fig. 1) corresponding to water bodies or dense canopy of trees. In this case, at the X-band, the true coherence between successive acquisitions should be zero due to a combination of rapid temporal and volumetric decorrelation effects and all

Fig. 1. High-resolution spotlight SAR amplitude image of the Eisenbahn bridge in Berlin acquired by a TerraSAR-X satellite sensor.

eigenvalues should be equal to the noise variance. However, due to bias in the estimation of the true coherence, the empirical coherence matrix will have random nonzero, nondiagonal entries of small magnitude.

The eigenvalue spectrum obtained by performing an EVD on a coherence matrix corresponding to different types of scatterers for simulated and real data is shown in Fig. 2. We observe that the magnitude of eigenvalue contributions (percentage contribution of individual eigenvalues for a coherence matrix) for the simulated noise case [Fig. 2(a)] and those corresponding to completely decorrelated pixels from real SAR data [Fig. 2(b)] are identical. For the rest of this paper, the percentage eigenvalue contribution will be referred to as eigenvalue. From the data, it is also seen that in the case of PS [Fig. 2(c)], the top eigenvalue is significantly large, whereas the rest of the eigenvalues are almost equal to zero. In the case of pixels containing multiple (we shall only consider the case of two scatterers in a pixel for this paper) scatterers [Fig. 2(d)], two significantly large eigenvalues are observed. Theoretically, for a covariance matrix of data containing noise and signal, few eigenvalues should have large magnitude proportional to the signal correlation. The remaining eigenvalues will be small and of equal magnitude proportional to the noise variance. This is not observed in the eigenvalue spectrum for noise pixels [Fig. 2(a) and (b)]. Any target detection rule based solely on the eigenvalue spectrum, such as the Kaiser–Guttman greater-than-one rule [29], will work for highly coherent targets with a few large eigenvalues but overestimate the number of significant eigenvalues in the spectrum in the case of low coherence and noise pixels.

Random matrix theory has been successfully used in many fields of mathematics and financial time-series processing to explain the nature of covariance matrices. Such an approach allows us to represent the covariance/coherence matrices as random processes and analytically obtain the jpdf of eigenvalues. This allows us to understand the interactions between eigenvalues, which gives rise to the observed eigenvalue spectrum and renders an explanation for the few large eigenvalues observed for noise pixels.

For our null model simulating a decorrelated pixel, we can directly state the results for jpdf of eigenvalues for large N value as given in [29]

$$P(\Lambda_1, \Lambda_2, \ldots, \Lambda_N) = \frac{1}{\exp\left(\frac{-3\beta N^2}{4}\right)} \exp\left(-\left(\frac{\beta}{2}\right)\sum_{i=1}^{N}\Lambda_i\right) \times \prod_{i=1}^{N}\Lambda_i^{\left(\frac{\beta}{2}\right)\left((1+L-N)-\frac{2}{\beta}\right)}\left|\prod_{j\neq k}\Lambda_j-\Lambda_k\right|^{\beta} \quad (5)$$

where $\beta = 2$ is the Dyson index for the complex case.

Equation (5) is seen as to be composed of two competing interactions. The upper half of the equation looks similar to a Gaussian process, whereas the lower half causes the value of the function to vary depending on the distance between pairs of eigenvalues. Reference [30] has employed a Coulomb gas analogy to explain this phenomenon. The value of the jpdf decreases when the eigenvalues get very close to each other, whereas the probability of having eigenvalues spaced apart increases. Thus, it can be inferred that the eigenvalues of a coherence matrix for a random Gaussian process tend to move away from each other giving a spectrum of unequal eigenvalues. This is the reason why the observed eigenvalues for the null case are not equal in magnitude. Fig. 3(a) gives the histogram of all eigenvalues for the simulated null case. The histogram follows the Marchenko–Pastur distribution. As the eigenvalues get closer to each other in magnitude, the probability of such an event decreases. Also, the ripple in the distribution suggests that the large magnitude eigenvalues of noise prefer to occupy discrete values causing local reduction in density.

With regard to the statistical response of the top eigenvalue for the null case, as shown in [29] and [34], the asymptotic distribution of largest eigenvalue follows a Tracy–Widom distribution. This is seen in Fig. 4 after median location and deviation from median (MAD) scale transformation have been applied to the top eigenvalue for 10 000 simulation runs. The top eigenvalue for the noise pixels in the real SAR data should fall within the range of the Tracy–Widom distribution. This will not be true in the case of pixels containing a stable target. The top eigenvalues for these pixels will exceed this threshold. For the purpose of our analysis, we set the threshold to 3.5 MAD ($\Lambda = 25\%$) from Fig. 4. The false alarm rate is 0.5%.

B. Eigenvalue Thresholding Scheme Applied to Real Data

From the Berlin SAR data, pixels whose top eigenvalue is less than the threshold are qualified as noise pixels and the histogram of the eigenvalue spectrum is shown in Fig. 3(b). The results are strikingly similar to the one expected from Fig. 3(a) using simulated data. In Fig. 3(c), we plot the eigenvalue density for pixels qualified as a PS. The probability density is seen to be composed of two parts, one containing eigenvalues corresponding to stable targets [Fig. 3 (right column)] and the other containing the eigenvalues representing noise. Incidentally, Fig. 3 (left column) of the eigenvalue distribution looks similar to the eigenvalue distribution for the null case. Thus, we can infer that the eigenvalues corresponding to decorrelation arrange themselves according to the jpdf for the random matrix model. In the case of multiscatterer pixels

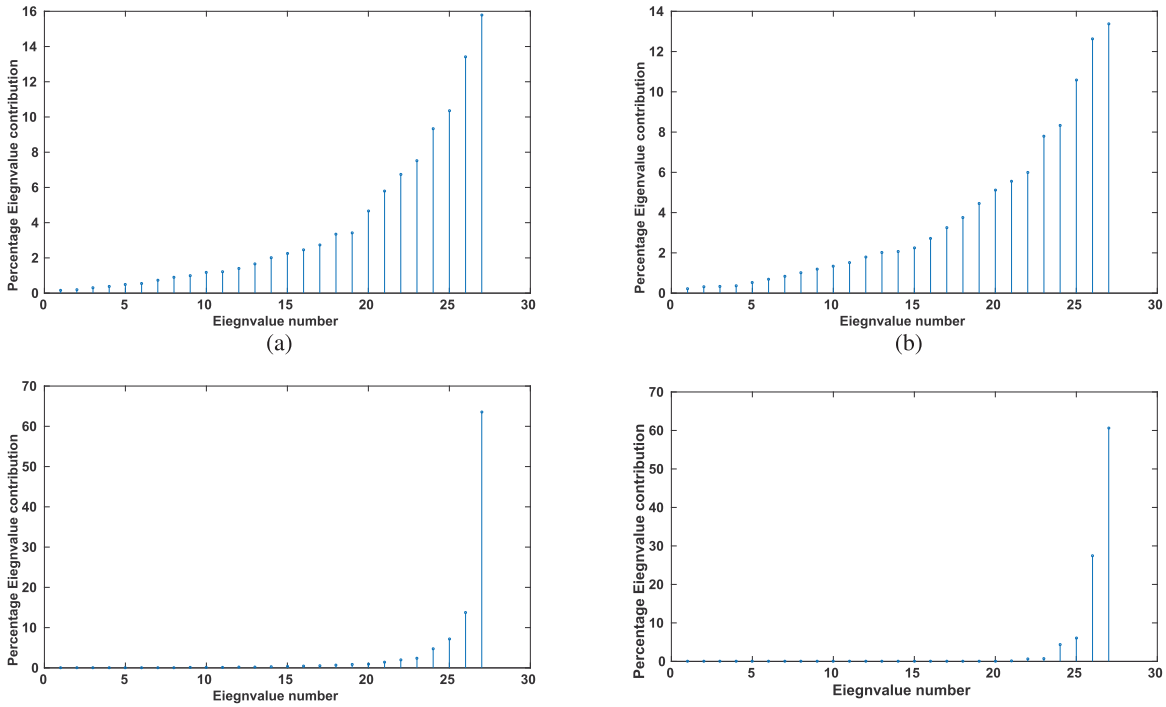

Fig. 2. Contribution of eigenvalues for different scatterer types. The x-axis represents the eigenvalue and the y-axis represents the eigenvalue contribution. (a) Simulated noise using random matrix theory. (b) Real data pixels corresponding to noise. (c) Real data pixels corresponding to PS. (d) Real data multiscatterer pixels affected by two target layovers.

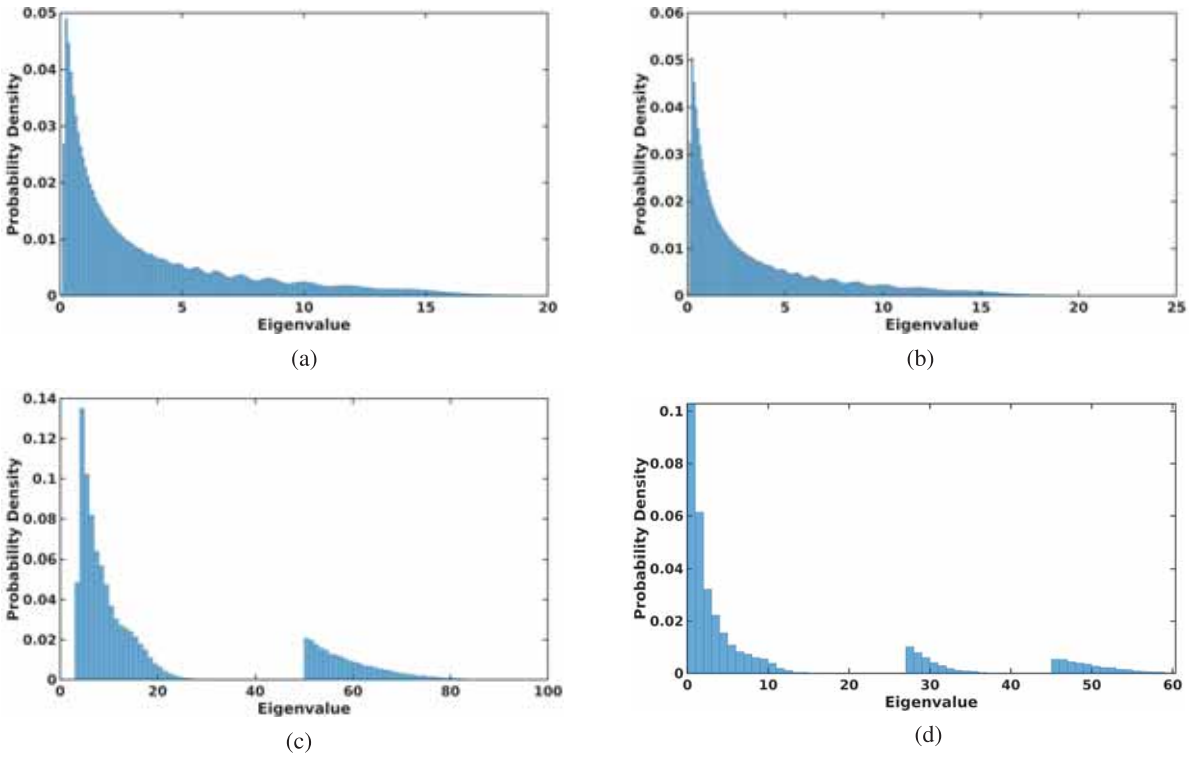

Fig. 3. Histogram of all eigenvalues of the coherence matrix for different types of scatterers. The x-axis represents the eigenvalue and the y-axis represents the probability density. (a) Simulated noise using the random matrix theory. (b) Real data pixels corresponding to noise. (c) Real data pixels corresponding to a PS. (d) Real data multiscatterer pixels affected by two target layovers.

having another secondary target, the top two eigenvalues are of comparable magnitude. The joint probability density is composed of three parts as seen in Fig. 3(d), two distributions representing two individual targets with the primary eigenvalue having greater or comparable magnitude to the secondary eigenvalue.

This technique can be used to discriminate stable scattering targets having a distinct distribution in comparison with noise. Also, it is very effective in identifying layover-affected pixels, which have the presence of more than one PS. The phase of the eigenvector corresponding to the eigenvalue of the target of interest can be used to filter the original interferogram phase.

The StaMPS temporal coherence is a measure of the temporal variation of the residual phase of a pixel obtained by spatially filtering its phase with neighboring candidates assuming deformation and noise artifacts, such as orbital error and atmosphere, are spatially correlated

$$\gamma_x = \frac{\left|\sum_{i=1}^{N} \exp\left[j\left(\phi_{\text{int\_orig},x,i} - \tilde{\phi}_{\text{mean\_est},x,i} - \hat{\phi}_{x,i}^{\text{not\_corr}}\right)\right]\right|}{N} \tag{6}$$

where $\phi_{\text{int\_orig},x,i}$ is the original interferometric phase for the x_{th} candidate in the i_{th} interferogram, $\tilde{\phi}_{\text{mean\_est},x,i}$ is the mean estimate of correlated phase (LoS deformation, atmospheric, and orbital errors), and $\hat{\phi}_{x,i}^{\text{not\_corr}}$ is the estimate for the non-correlated phase (residual DEM artifacts and noise).

The accuracy of measured residual phase is dependent on the filtered phase estimate from neighboring candidates. In the case of scatterers surrounded by noise, the temporal coherence is underestimated. Also, in Fig. 5(a), it is inferred that the temporal coherence is overestimated (0.1–0.3) for pixels corresponding to noise such as those on water. Although pixels corresponding to double bounce of bridge have high SNR as seen from Fig. 1, they are indistinguishable from noise in the temporal coherence map. In the StaMPS PS selection process, the probability that a candidate pixel is a PS is proportional to the magnitude of the temporal coherence. It performs well when detecting a PS having high temporal coherence (>0.3) [Fig. 5(b)], still quite a number of false alarms in water have been detected, suggesting that an even higher threshold should be imposed. Relaxing the threshold on the temporal coherence for PS selection (>0.20) only introduces more false alarms [Fig. 5(c)] without increasing measurement points for the bridge section and double bounce. Fig. 5(d) shows the results for our eigenvalue thresholding to qualify pixels as stable candidates. Most of the false alarms detected using a temporal coherence threshold have been rejected by our selection strategy. This shows that even though there is a bias in empirical coherence, the statistical properties of the top eigenvalue of a random matrix model can be used to identify and reject these pixels. In addition, the low coherence bridge section and the pixels corresponding to double bounce have been selected. The eigenvalue thresholding strategy reveals a highly contextual relationship between the eigenvalues and the pixel they represent.

For further time-series analysis, we will assume only one scatterer represented by the highest eigenvalue per pixel. The 3-D phase unwrapping procedure as described in [35] is used in this paper.

IV. Time-Series Analysis

The time-series analysis using the PS approach [36] reveals a combination of periodic and linear deformation in Berlin

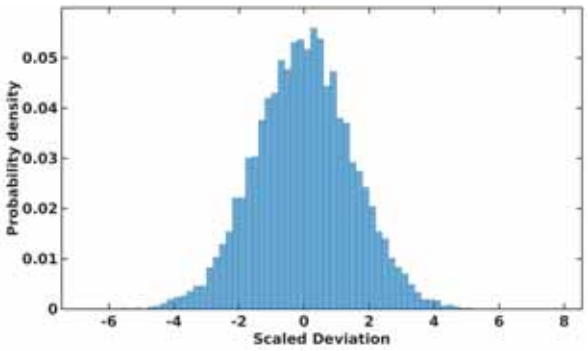

Fig. 4. Distribution of top eigenvalue of coherence matrix. The 10 000 simulation runs for noise (after median and MAD location and scale transformation). The median is 18.43 and MAD is 1.02.

for the Eisenbahn railway bridge. Seasonal variation of temperature causes the bridge to expand during the summer and contract during winter. This causes a periodic deformation pattern evident in the results published in [37] (around 10 mm). 3-D geodetic mapping and decomposition of the InSAR deformation is performed using a combination of ascending and descending pass images [37]. However, it is also seen that there is an absence of PS points over the western section of the lower bridge Fig. 1 primarily in ascending track [36], [37]. Therefore, it will be difficult to obtain 3-D deformation estimates for PS, which are only visible from a single imaging track. This is usually true for PS points of targets in shadow regions in the SAR images from one of the tracks, but this is not the case for the Eisenbahn bridge which is clearly visible from both the tracks.

There is also a lack of the literature discussing the detection of PS points on the double bounce for this bridge, which is observed in the amplitude data (Fig. 1). The first returns from a bridge will appear to be closer to a radar in the focused SAR image than its original position (at the point on water directly below the bridge) in proportion to the height of the bridge above the water surface. The double bounce, however, is due to the reflection of the radar signal from the bridge to the water before arriving at the receive antenna of the radar. These returns will be focused to the original position of the bridge above the water surface. These returns are a combination of stable scattering from targets on the bridge in addition to a decorrelation effect due to the scattering from the water surface. The decorrelation caused due to the scattering from the water surface is the primary reason why no PSs are detected even though the returns appear extremely bright and stable in the amplitude image. This is confirmed from our analysis using the StaMPS approach, which reveals that the missing sections of the bridge and double bounce have low temporal coherence measure [Fig. 5(a)]. The average deformation rate estimate using StaMPS is shown in Fig. 6 whereas that using our pixel selection strategy is shown in Fig. 7.

Several differences can be noted.

1) The total number of measurement points detected by StaMPS is 48 259 (Fig. 6) and those detected using our selection strategy is 220 914 (Fig. 7) which is 4.5 times increase in measurement point density.

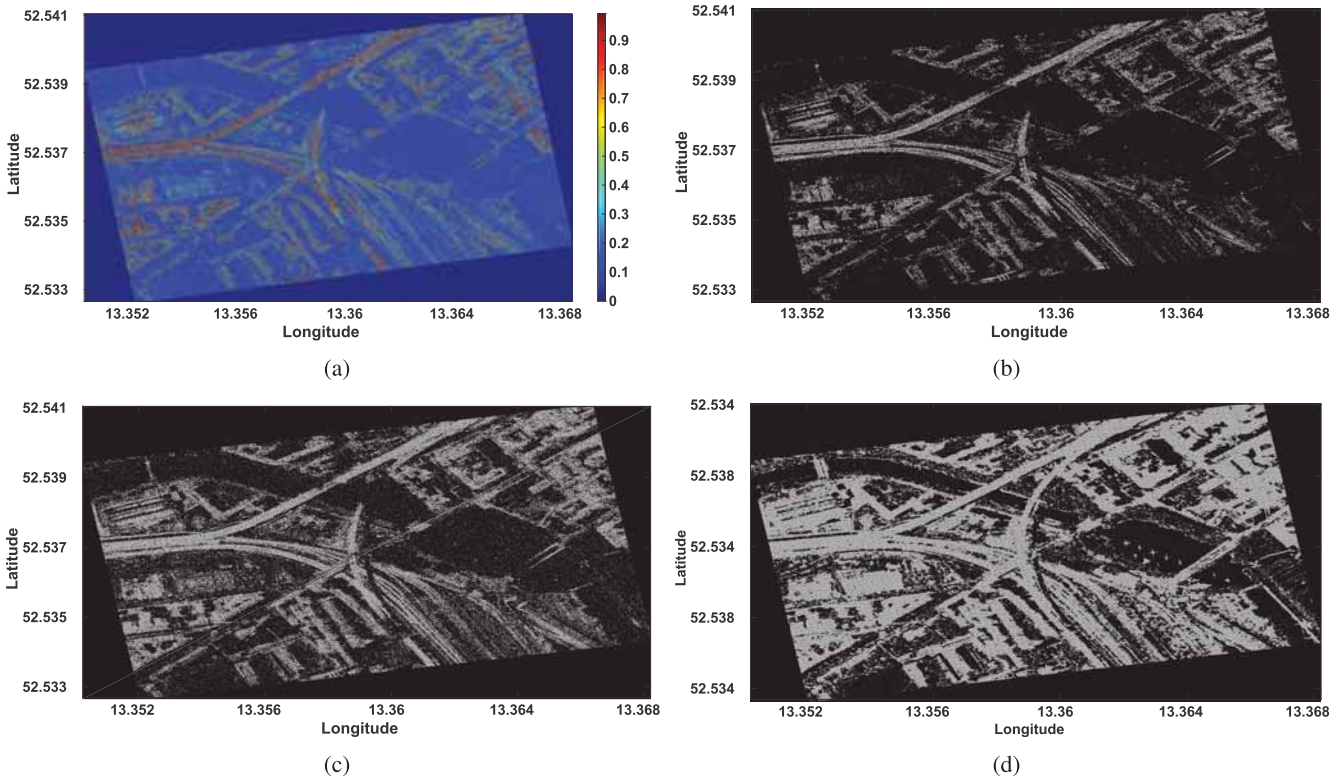

Fig. 5. (a) Temporal coherence obtained after processing the Berlin SAR data in StaMPS. The double bounce and a section of the bridge seem to have very low temporal coherence equivalent to water pixels. (b) Total pixels selected for phase unwrapping with temporal coherence threshold >0.3. (c) Total pixels selected for phase unwrapping with a temporal coherence threshold >0.2. (d) Total pixels selected for phase unwrapping using our eigenvalue thresholding scheme.

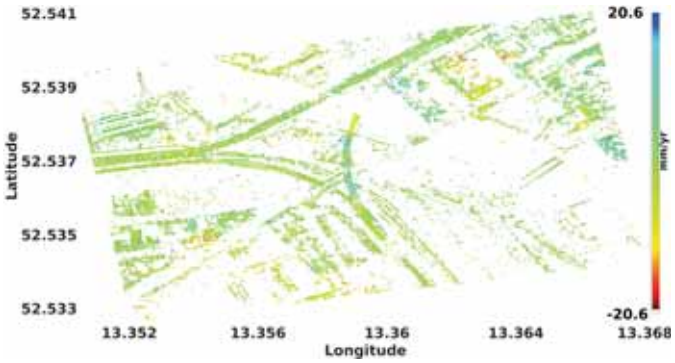

Fig. 6. Average LoS deformation velocity for the Berlin data using traditional StaMPS processing.

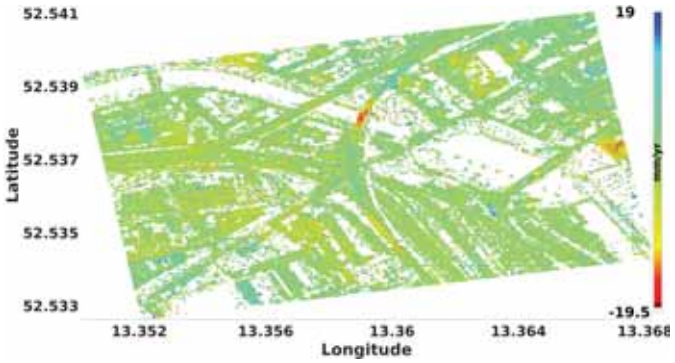

Fig. 7. Average LoS deformation velocity for the Berlin data using eigenvalue thresholding scheme processing.

2) Our capability to discern between low coherence pixels and noise has dramatically improved with the increased number of detected points over the low coherence regions. In addition, we have been able to identify new regions in the image including the west section of bridge and double bounce reflections of the bridge. This is the first time that double bounce detection in the time-series analysis is being reported.
3) The false detection of stable targets over water pixels in the case of StaMPS is completely rejected with our selection strategy [Fig. 5(b)–(d)].
4) Our algorithm also gives us the flexibility to select from multiple targets from within layover-affected pixels. These pixels are usually rejected in traditional time-series processing, because targets undergoing variable motion within the same pixel tend to reduce the coherence of the pixel.
5) Targets present in water surrounded by noisy pixels are also rejected in traditional processing due to their low temporal coherence. Such pixels are now selected in our processing [Fig. 5(c) and (d)].

The missing portion of the bridge as seen in Fig. 1 but for which no PS have been found in Fig. 6 is seen to be composed of two sections of the bridge resting on a pillar. One section is part of the bridge above water, whereas the other is part of the section attached to the ground. From Fig. 6, it is clear that the bridge above water is experiencing deformation, whereas the sections attached to the ground are stable. From our results in Figs. 7 and 8, we see that the new PS points found on the missing segments of the

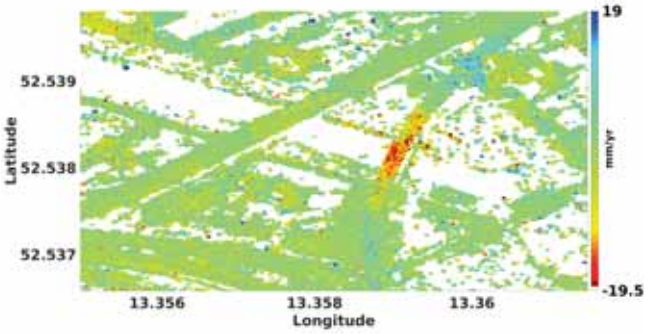

Fig. 8. Average LoS deformation velocity for the Berlin data using eigenvalue thresholding scheme processing (cropped from Fig. 7 to show the detection of the missing bridge section and double bounce response of a bridge).

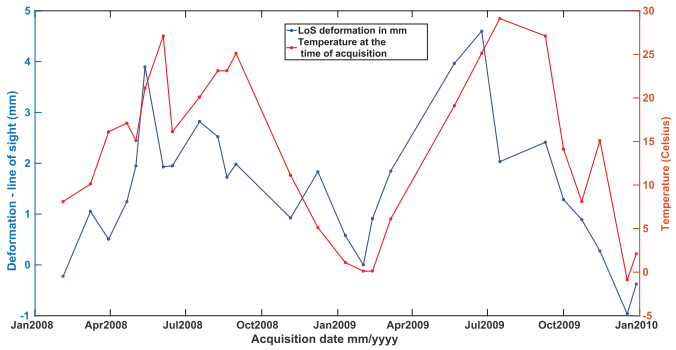

Fig. 9. Time-series LoS deformation for the Berlin data using eigenvalue thresholding scheme processing showing seasonal deformation over a two−year acquisition period (February 2008−−December 2009).

bridge in Fig. 6 experience the similar deformation to their corresponding sections (above water or connected to ground) for which PS information is available in Fig. 6, thus validating our hypothesis that there was meaningful information, which could be extracted from these pixels if we found a way to differentiate them from noise. Similarly, the new PS found on the section of the bridge connected to the ground is found to be stable.

Due to a combination of linear and seasonal motion, it appears as if the bridge above the water is moving toward the radar sensor, whereas the rest of it is stable. Purely seasonal deformation can be clearly observed in Fig. 9. In [36], this has been related to the coefficient of thermal expansion and the maximum temperature difference. These results corroborate with the findings of this paper.

The time-series plot in Fig. 9 shows the LoS deformation for PS showing zero average deformation over the two-year acquisition period. The left-hand y-axis shows the deformation of the scatterers in millimeters, whereas the right-hand y-axis shows the temperature in Celcius at the time of the acquisition. There is a clear trend in seasonal variation in temperature, which causes the thermal expansion of material used in construction of the bridge, which reflects in the time-series deformation estimate. It can be seen that the largest disagreement would be around a few millimeters. This can arise due to multiple reasons. First, the weather station is located at the Berlin airport, which is around 10 km from the InSAR measurement site of concern (Eisenbahn Bridge), which could locally have a different temperature. Second, the ambient temperature may also change with regard to the height of the InSAR PS scatterer (points on the bridge). Third, some atmospheric error might be leaked into the deformation measurement during the time-series processing.

Finally, it should be noted that the spotlight data set is chosen, because it has a high density of the PS and the DS as well as multitarget layover pixels. The river in the test site and shadow created by the bridges are ideal regions to test the decorrelation model. Numerous publications [36], [37] on the time-series analysis using multiple techniques (PS, SBAS, Tomography, and so on) with this particular data set helped in calibrating the algorithm. Also, this paper primarily came out of trying to address the problem of the missing section of the bridge due to low coherence using conventional time-series InSAR techniques as shown in this paper, which was a recurring problem in all prior publications. However, the feasibility of the proposed technique on middle-resolution SAR imagery is a great topic for further research.

V. Conclusion

PSInSAR processing is a powerful tool for performing continuous, wide-scale, and precise deformation monitoring for a host of geophysical phenomena. Several algorithms, such as SBAS, SqueeSAR (DS), and CAESAR, have been touted to improve the number of measurement points obtained for stable, layover, and slow decorrelation environments. The primary metric used to qualify pixels for phase unwrapping is the average magnitude of temporal coherence over the interferogram stack. These techniques perform well when detecting measurement points over stable high-coherence regions but provide poor results over regions of low temporal coherence, because noisy pixels may also have comparable temporal coherence due to the bias in the coherence estimation.

In this paper, we have developed a model for decorrelation based on recent advances in the random matrix theory. It has been shown that the probability distribution of all eigenvalues of the coherence matrix for a pixel is limited by the Marchenko–Pastur distribution and gives far more information about the decorrelating nature of a pixel in comparison with purely the eigenvalue spectrum of the coherence matrix. The top eigenvalue of the spectrum follows a Tracy–Widom-like distribution. The random matrix model inherently captures the bias in the temporal coherence, which affect the statistics of the jpdf and top eigenvalue. Therefore, we can apply a threshold on the top eigenvalue of the coherence matrix spectrum to qualify pixels as stable or decorrelated scatterers.

Our time-series analysis results over the Eisenbahn bridge in Berlin show the substantial increase in measurement points over low-coherence regions. The results not only demonstrate an increase in measurement point density, but also the advantage of obtaining measurement points over regions unidentified by other algorithms (missing region of the bridge and double bounce). These results are indicative of the performance improvement obtained by looking at InSAR as a random matrix theory phenomena instead of the traditional temporal coherence model. We are able to present a technique to pick stable pixels from interferogram stacks. However, the time-series analysis may require filtering of the

InSAR measurement prior to phase unwrapping. We suggest a CAESAR-like filtering [28] to be performed on the selected pixels before time-series estimation. Since both techniques involve EVD, a PCA-based filtering technique can be integrated into the current processing scheme.

It is possible that seasonally coherent scatterers as well as temporary scatterers may provide relevant deformation information only over a subset of the total period for which the time-series processing is desired. Based on the coherence interferograms of small baseline pairs, for every pixel, the number of SAR images involved in the covariance matrix estimate can be changed. Further research will focus on improving the random matrix model to include large-tail distributions and characterizing the statistical properties of jpdf of eigenvalues representing numerous scattering mechanisms, in addition to improving the computational efficiency of the algorithm.

ACKNOWLEDGMENT

The authors would like to thank the German Aerospace Agency (DLR) for providing TerraSAR-X data for the purpose of this paper. TerraSAR-X data are copyright of DLR and provided via Project LAN3188.

REFERENCES

[1] M. Simons and P. Rosen, "Interferometric synthetic aperture radar geodesy," in *Treatise on Geophysics: Geodesy*, vol. 3, 2nd ed. Amsterdam, The Netherlands: Elsevier, 2007, pp. 391–446.

[2] Z. Lu and D. Dzurisin, *InSAR Imaging of Aleutian Volcanoes: Monitoring a Volcanic Arc From Space* (Springer Praxis Books/Geophysical Sciences). Berlin, Germany: Springer, 2014.

[3] R. Touzi, A. Lopes, J. Bruniquel, and P. W. Vachon, "Coherence estimation for SAR imagery," *IEEE Trans. Geosci. Remote Sens.*, vol. 37, no. 1, pp. 135–149, Jan. 1999.

[4] H. A. Zebker and J. Villasenor, "Decorrelation in interferometric radar echoes," *IEEE Trans. Geosci. Remote Sens.*, vol. 30, no. 5, pp. 950–959, Sep. 1992.

[5] R. F. Hanssen, *Radar Interferometry: Data Interpretation and Error Analysis*. Berlin, Germany: Springer, 2001.

[6] D. Massonnet and K. L. Feigl, "Radar interferometry and its application to changes in the Earth's surface," *Rev. Geophys.*, vol. 36, no. 4, pp. 441–500, 1998.

[7] G. W. Bawden, W. Thatcher, R. S. Stein, K. W. Hudnut, and G. Peltzer, "Tectonic contraction across Los Angeles after removal of groundwater pumping effects," *Nature*, vol. 412, no. 6849, pp. 812–815, 2001.

[8] F. Cigna, E. Cabral-Cano, B. Osmanoglu, T. H. Dixon, and S. Wdowinski, "Detecting subsidence-induced faulting in Mexican urban areas by means of Persistent Scatterer Interferometry and subsidence horizontal gradient mapping," in *Proc. IEEE Int. Geosci. Remote Sens. Symp.*, Jul. 2011, pp. 2125–2128.

[9] F. Qu, Z. Lu, M. Poland, J. Freymueller, Q. Zhang, and H.-S. Jung, "Post-eruptive inflation of Okmok volcano, Alaska, from InSAR, 2008–2014," *Remote Sens.*, vol. 7, no. 12, pp. 16778–16794, 2015.

[10] A. Ferretti, C. Prati, and F. Rocca, "Permanent scatterers in SAR interferometry," *IEEE Trans. Geosci. Remote Sens.*, vol. 39, no. 1, pp. 8–20, Jan. 2001.

[11] A. Hooper, H. Zebker, P. Segall, and B. Kampes, "A new method for measuring deformation on volcanoes and other natural terrains using InSAR persistent scatterers," *Geophys. Res. Lett.*, vol. 31, no. 23, pp. 6–11, Dec. 2004.

[12] B. M. Kampes, *Radar Interferometry: Persistent Scatterer Technique*. Dordrecht, The Netherlands: Springer-Verlag, 2006.

[13] N. Adam, B. Kampes, M. Eineder, J. Worawattanamateekul, and M. Kircher, "The development of a scientific permanent scatterer system," presented at the ISPRS Hannover Workshop, Hanover, Germany, Oct. 2003.

[14] Z. Lu and O.-I. Kwoun, "Radarsat-1 and ERS InSAR analysis over southeastern coastal Louisiana: Implications for mapping water-level changes beneath swamp forests," *IEEE Trans. Geosci. Remote Sens.*, vol. 46, no. 8, pp. 2167–2184, Aug. 2008.

[15] P. Berardino, G. Fornaro, R. Lanari, and E. Sansosti, "A new algorithm for surface deformation monitoring based on small baseline differential SAR interferograms," *IEEE Trans. Geosci. Remote Sens.*, vol. 40, no. 11, pp. 2375–2383, Nov. 2002.

[16] A. Ferretti, A. Fumagalli, F. Novali, C. Prati, F. Rocca, and A. Rucci, "A new algorithm for processing interferometric data-stacks: SqueeSAR," *IEEE Trans. Geosci. Remote Sens.*, vol. 49, no. 9, pp. 3460–3470, Sep. 2011.

[17] G. Fornaro and F. Serafino, "Imaging of single and double scatterers in urban areas via SAR tomography," *IEEE Trans. Geosci. Remote Sens.*, vol. 44, no. 12, pp. 3497–3505, Dec. 2006.

[18] C. Rossi and M. Eineder, "High-resolution InSAR building layovers detection and exploitation," *IEEE Trans. Geosci. Remote Sens.*, vol. 53, no. 12, pp. 6457–6468, Dec. 2015.

[19] C. Dubois, A. Thiele, A. Welte, and S. Hinz, "Parameterisation of layover detector for urban analysis in InSAR data," in *Proc. IEEE JURSE*, Mar./Apr. 2015, pp. 1–4.

[20] F. Baselice, A. Budillon, G. Ferraioli, and V. Pascazio, "Joint SAR imaging and DEM reconstruction from multichannel layover-affected SAR data," in *Proc. IEEE Int. Geosci. Remote Sens. Symp.*, Jul. 2009, pp. III-25–III-28.

[21] F. Cellier and E. Colin, "Building height estimation using fine analysis of altimetric mixtures in layover areas on polarimetric interferometric X-band SAR images," in *Proc. IEEE Int. Geosci. Remote Sens. Symp.*, Jul./Aug. 2006, pp. 3987–3990.

[22] X. X. Zhu and R. Bamler, "Very high resolution spaceborne SAR tomography in urban environment," *IEEE Trans. Geosci. Remote Sens.*, vol. 48, no. 12, pp. 4296–4308, Dec. 2010.

[23] F. Lombardini, "Differential tomography: A new framework for SAR interferometry," *IEEE Trans. Geosci. Remote Sens.*, vol. 43, no. 1, pp. 37–44, Jan. 2005.

[24] A. Reigber and A. Moreira, "First demonstration of airborne SAR tomography using multibaseline L-band data," *IEEE Trans. Geosci. Remote Sens.*, vol. 38, no. 5, pp. 2142–2152, Sep. 2000.

[25] F. Lombardini and M. Pardini, "Superresolution differential tomography: Experiments on identification of multiple scatterers in spaceborne SAR data," *IEEE Trans. Geosci. Remote Sens.*, vol. 50, no. 4, pp. 1117–1129, Apr. 2012.

[26] D. Reale, G. Fornaro, and A. Pauciullo, "Extension of 4-D SAR imaging to the monitoring of thermally dilating scatterers," *IEEE Trans. Geosci. Remote Sens.*, vol. 51, no. 12, pp. 5296–5306, Dec. 2013.

[27] G. Fornaro, D. Reale, and F. Serafino, "Four-dimensional SAR imaging for height estimation and monitoring of single and double scatterers," *IEEE Trans. Geosci. Remote Sens.*, vol. 47, no. 1, pp. 224–237, Jan. 2009.

[28] G. Fornaro, S. Verde, D. Reale, and A. Pauciullo, "CAESAR: An approach based on covariance matrix decomposition to improve multibaseline–multitemporal interferometric SAR processing," *IEEE Trans. Geosci. Remote Sens.*, vol. 53, no. 4, pp. 2050–2065, Apr. 2015.

[29] D. C. Hoyle and M. Rattray, "Principal-component-analysis eigenvalue spectra from data with symmetry-breaking structure," *Phys. Rev. E, Stat. Phys. Plasmas Fluids Relat. Interdiscip. Top.*, vol. 69, no. 2, p. 026124, Feb. 2004.

[30] S. N. Majumdar and P. Vivo, "Number of relevant directions in principal component analysis and Wishart random matrices," *Phys. Rev. Lett.*, vol. 108, p. 200601, May 2012.

[31] A. Parizzi and R. Brcic, "Adaptive InSAR stack multilooking exploiting amplitude statistics: A comparison between different techniques and practical results," *IEEE Geosci. Remote Sens. Lett.*, vol. 8, no. 3, pp. 441–445, May 2011.

[32] Z. D. Bai, "Methodologies in spectral analysis of large dimensional random matrices: A review," *Statist. Sinica*, vol. 9, no. 3, pp. 611–662, 1999.

[33] E. Erten, "The performance analysis based on SAR sample covariance matrix," *Sensors*, vol. 12, no. 3, pp. 2766–2786, 2012.

[34] K. Johansson, "Shape fluctuations and random matrices," *Commun. Math. Phys.*, vol. 209, no. 2, pp. 437–476, Feb. 2000.

[35] A. Hooper and H. A. Zebker, "Phase unwrapping in three dimensions with application to InSAR time series," *J. Opt. Soc. Amer. A, Opt. Image Sci.*, vol. 24, no. 9, pp. 2737–2747, 2007.

[36] S. Gernhardt and R. Bamler, "Deformation monitoring of single buildings using meter-resolution SAR data in PSI," *ISPRS J. Photogramm. Remote Sens.*, vol. 73, pp. 68–79, Sep. 2012.

[37] S. Montazeri, X. X. Zhu, M. Eineder, R. F. Hanssen, and R. Bamler, "Deformation monitoring of urban infrastructure by tomographic SAR using multi-view TerraSAR-X data stacks," presented at the Fringe, Adv. Sci. Appl. SAR Interferometry Sentinel-1 InSAR Workshop, Frascati, Italy, Mar. 2015, doi: 10.5270/Fringe2015.314.

Sankarambadi Navneet received the master's degree in geophysics from Southern Methodist University, Dallas, TX, USA, in 2017.

He is currently with Capella Space Corp., Palo Alto, CA, USA, where he is involved in building a constellation of low-cost, small-cubage, and high-resolution synthetic aperture radar (SAR) satellites. His research interests include SAR imaging algorithms and interferometric SAR time-series processing techniques.

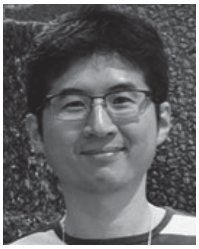

Jin-Woo Kim received the B.S. and M.S. degrees in civil engineering from Yonsei University, Seoul, South Korea, in 2005 and 2007, respectively, and the Ph.D. degree in geodetic science from The Ohio State University, Columbus, OH, USA, in 2013.

He is currently a Staff Scientist with the Roy M. Huffington Department of Earth Sciences, Southern Methodist University, Dallas, TX, USA, where he is investigating the earth surface processes with SAR imagery and InSAR methods. His research interests include InSAR applications to understand wetland hydrology, sinkhole evolution, landslide mechanisms, and interactions between human activities and surface/underground processes.

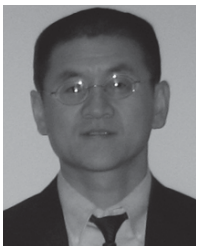

Zhong Lu (M'97–SM'07) received the B.S. and M.S. degrees from Peking University, Beijing, China, in 1989 and 1992, respectively, and the Ph.D. degree from the University of Alaska Fairbanks, Fairbanks, AK, USA, in 1996.

He was a Physical Scientist with the U.S. (USGS) Geological Survey from 1997 to 2013. He is currently a Professor and the Endowed Shuler-Foscue Chair with the Roy M. Huffington Department of Earth Sciences, Southern Methodist University, Dallas, TX, USA. He is a Principal Investigator of projects funded by the U.S. National Aeronautics and Space Administration, the European Space Agency, the Japan Aerospace Exploration Agency (JAXA), the German Aerospace Agency (DLR), and the USGS, focused on the study of land surface deformation using satellite InSAR imagery. He has produced over 45 lead-authored and 105 co-authored peer-reviewed journal articles and book chapters focused on InSAR techniques and applications. He is a co-author of a book *InSAR Imaging of Aleutian Volcanoes: Monitoring a Volcanic Arc from Space* (Springer, 2014). His research interests include the technique developments of SAR, InSAR, and persistent scatterer InSAR processing and their applications on volcanoes, landslides, and coastal processes among others.

Dr. Lu is a Committee Member of Western North America InSAR Consortium, NASA's Alaska Satellite Facility User Working Group, and the upcoming NASA-India SAR Science Definition Team. He was a recipient of the Ford Senior Research Fellowship, the American Society for Photogrammetry and Remote Sensing Award for Best Scientific Paper in Remote Sensing, the NASA Group Achievement Award, the NASA Certificate of Appreciation, the Raytheon Distinguished Level Award for Excellence in Technology, the Science Applications International Corporation Technical Fellow, and the Jerald Cook Memorial Award. He is an Associate Editor of *Remote Sensing* and *Frontier in Volcanology*, and a member of editorial boards of the *International Journal of Image and Data Fusion* and *Geomatics, Natural Hazards and Risk*.